GLOBAL MODES IN COMPRESSIBLE JETS

X. Garnaud*[1], L. Lesshafft[1], P. Schmid[1], P. Huerre[1]

[1] Laboratoire d'Hydrodynamique, Ecole Polytechnique
91128 Palaiseau cedex, France
* Corresponding author: garnaud@ladhyx.polytechnique.fr

This paper presents first results from a global stability analysis of subsonic jets. Global modes of the linear compressible Navier–Stokes equations are computed for one isothermal and one hot jet configuration at Re = 100 and Ma = 0.9. The spatial structure of global mode wave packets is obtained together with their frequencies and temporal growth rates. Several families of global modes are identified, and characteristic features of their near-field dynamics are discussed. The computations are designed to encompass the acoustic far-field of the global modes. Far-field results are presented for one mode where the acoustic source region is fully contained within the computational domain.

1 Introduction

The sound that is emitted from subsonic jets is commonly attributed to two distinct aeroacoustic source mechanisms. On the one hand, turbulent fluctuations in the jet that are characterized by short coherence lengths emit a broad-band noise. On the other hand, coherent large-scale instability waves develop within the slowly varying mean flow of the jet, radiating a low-frequency tonal spectrum. Numerous investigations (recent studies include [4, 9]) demonstrate that the low-frequency emission due to instability waves contains the largest part of the radiated acoustic energy.

Numerical as well as experimental jet studies, over a wide range of operating conditions, consistently identify strong oscillations inside the jet at a fairly low frequency, known as the *preferred mode*. The acoustic signature of the preferred mode is usually found as a marked peak in the far field, particularly at radiation angles close to the jet axis. Ref. [10] gives a typical value of the Strouhal number $\mathrm{St}_d \approx 0.4$, based on jet diameter, for the preferred mode in round jets at low Mach number. Recent numerical simulations [4, 9] suggest a typical value between $\mathrm{St}_d = 0.2$ and 0.25 at high subsonic Mach numbers. [11] proposed an interpretation of the preferred mode as the least stable mode of a "slightly damped oscillator". The present study describes such slightly damped modes in a spatially varying jet.

Temporal global modes of the linearized compressible Navier–Stokes operator will be computed for subsonic isothermal and hot jet flows. The spatial structure of these eigenmodes encompasses both the near-field instability waves inside the jet and their acoustic radiation into the far field. The presence of the nozzle is accounted for; it is modeled as a straight pipe with an infinitely thin wall that extends into the computational domain.

Similar jet configurations were investigated in a nonlinear framework in ref. [12]. That study compared the simulated nonlinear jet dynamics to theoretical predictions based on *local* linear stability properties of the underlying base flow. The investigated parameters were necessarily limited to the absolutely unstable regime, i.e. to strongly heated jets, which were demonstrated to exhibit nonlinear global instability. The present study extends the scope of [12] in several important ways. First, globally stable settings such as isothermal jets can be considered. Secondly, in contrast to the earlier local stability analysis, the global modes immediately contain the acoustic signature of jet oscillations. Finally, the global approach fully accounts for the non-parallelism of the base flow, as well as for nozzle effects. However, comparison between linear global modes and nonlinear numerical simulations are not offered at this point, and sound generation is limited to linear source mechanisms.

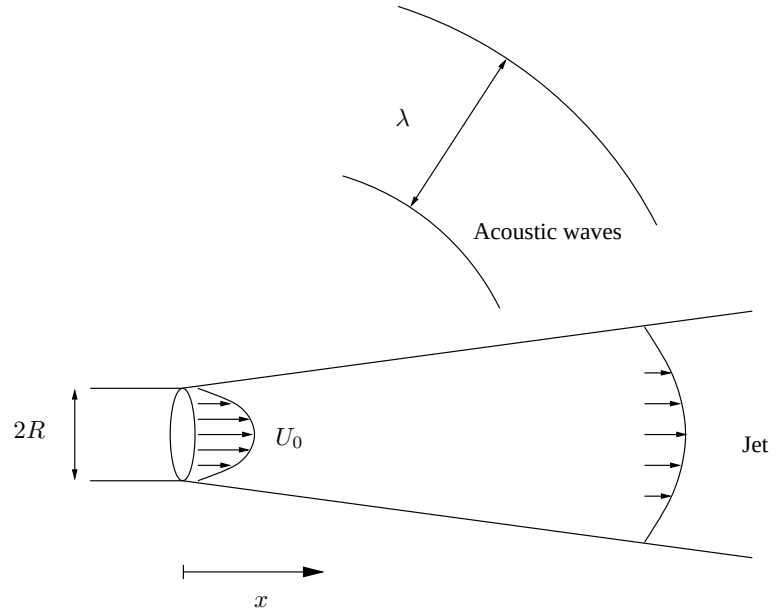

Figure 1: Flow configuration. The jet exits a cylindrical nozzle of radius R with an axial velocity U_0, a temperature T_0 and a density ρ_0. r and x respectively denote the radial and axial coordinates.

2 Flow model and numerical procedures

2.1 Governing equations and flow parameters

The flow is assumed to be governed by the compressible Navier–Stokes equations. In the present study, only axisymmetric flow perturbations are considered, and the equations are therefore cast in cylindrical coordinates (r, x), while all flow variables are taken to be constant along the azimuthal direction ϑ. The fluid is a perfect gas with adiabatic index $\gamma = 1.4$. In this paper, we consider temperature variations due to compressibility but also due to a possible difference between the jet temperature T_0 on the center-line and the ambient temperature T_∞. However, the fluid viscosity μ and thermal conductivity κ are assumed to be constant throughout the flow. The jet issues from a cylindrical nozzle of radius R at $x = 0$, as sketched in figure 1. At the nozzle exit, the flow is characterized by the center-line values of velocity U_0, temperature T_0 and density ρ_0. Together with the nozzle radius R, these reference values are used to non-dimensionalize the problem. The full equations are given in [12].

The heating of the jet is characterized by the ratio

$$S = \frac{T_\infty}{T_0}$$

which is here taken to be 1 (isothermal configuration) or 0.5 (hot jet). The jet operating conditions are further defined by the Reynolds, Mach and Prandtl numbers, which for the present study are chosen as

$$\mathrm{Re} = \frac{U_0 R \rho_0}{\mu} = 100, \qquad \mathrm{Ma} = \frac{U_0}{c_\infty} = 0.9, \qquad \mathrm{Pr} = \frac{\mu C_P}{\kappa} = 1,$$

where c_∞ denotes the ambient speed of sound and C_p is the specific heat at constant pressure.

In order to correctly capture the physics of the jet acoustics, the numerical domain contains the jet, a solid nozzle, a portion of the acoustic far-field and sponge layers, as shown in figure 2.

The computation of linear global modes involves two separate steps. First, a steady *base flow* must be obtained as a steady solution to the *nonlinear* equations of motion (section 2.3). Global modes are then computed as temporal eigenstates of the corresponding *linear* equations, linearized about the steady

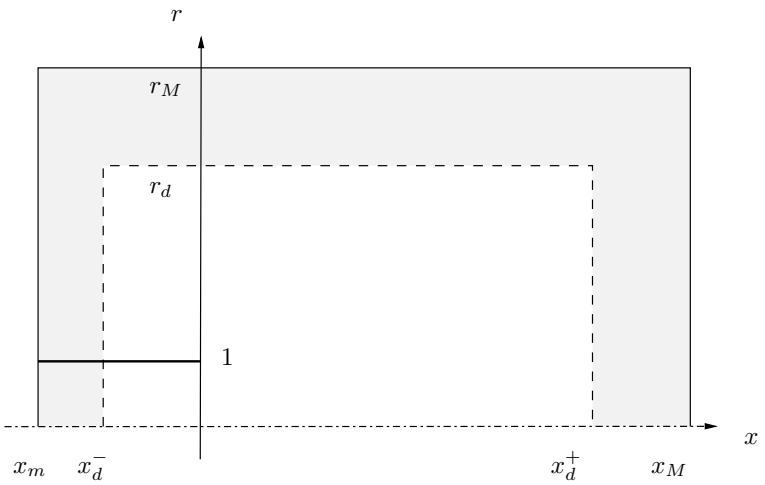

Figure 2: Computational domain defined by $x_m \le x \le x_M$ and $0 < r \le r_M$. The nozzle pipe is modeled by an infinitely thin solid wall at $r = 1$ and $x \le 0$. Sponge layers are represented in gray.

base flow (section 2.4).

2.2 Numerical discretization

Spatial derivatives in both the linear and nonlinear equations of motion are discretized using explicit sixth-order centered finite differences, and time integration is performed via a third-order Runge–Kutta algorithm. The highly accurate spatial scheme is required in order to minimize the dispersion and dissipation errors for acoustic wave propagation. Numerical instabilities of the finite-difference scheme arise in the high wave number regime. These are damped by applying a tenth-order accurate spatial filter procedure at regular intervals [14].

The computational domain covers the flow region over $-25 \le x \le 45$ and $0 < r \le 35$. The geometry is schematically drawn in figure 2. The singularity at $r = 0$ is avoided by placing the first radial grid point at half the local cell size away from the jet axis. The nozzle pipe is modeled as an infinitely thin wall at $r = 1$ that extends from the upstream domain boundary down to $x = 0$. The homogeneous governing flow equations are solved within the "physical region" $-10 \le x \le 30$ and $0 < r \le 20$ of the computational domain, whereas damping terms are added in the surrounding "sponge regions" (shaded gray in figure 2) in order to attenuate oscillations before they reach the computational boundaries. Despite the addition of a damping region, an accurate computation of acoustic wave propagation necessitates the use of high-quality non-reflecting boundary conditions [6]. Further details on the boundary treatment in the nonlinear (base flow) and the linear (global modes) computations are given in sections 2.3 and 2.4.

The present calculations use a non uniform rectilinear grid with 570×255 points in the (x, r) directions, with minimum spacing $\Delta x_{min} = \Delta r_{min} = 0.04$ in the vicinity of the nozzle lip. Throughout the physical region that contains 440×200 points, the grid sizes are no greater than $\Delta x_{max} = 0.1$ and $\Delta r_{max} = 0.2$. Strong grid stretching is applied in the sponge regions.

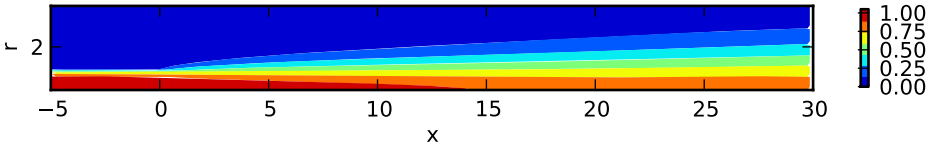

Figure 3: Axial velocity field for a steady isothermal base flow at Re = 100 and Ma = 0.9.

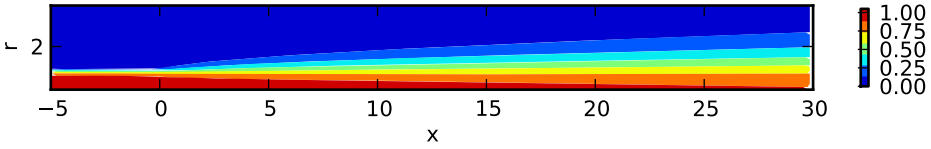

Figure 4: Axial velocity field for a steady hot base flow at Re = 100 Ma = 0.9 and $S = 0.5$.

2.3 Base flow

The shear layer thickness at the exit of the nozzle is known to be a critical parameter of the stability features of jet flows, and is thus desirable to control. This is done by imposing

$$\begin{cases} u_x = \begin{cases} \tanh\left(\frac{1-r(i)}{\phi}\right) & r \le 1 \\ 0 & r \ge 1 \end{cases} \\ u_r = 0 \\ u_\theta = 0 \\ p = \dfrac{1}{\gamma \mathrm{Ma}^2} \\ T = S + (1-S)u_x + \dfrac{\gamma-1}{2}\mathrm{Ma}^2 u_x(1-u_x) \end{cases} \tag{1}$$

at the inlet of the numerical domain, $x = x_m$. Such a profile is characterized by the heating parameter S and the characteristics length of the shear layer ϕ. A body force $\boldsymbol{F}(r)$ is added to the Navier–Stokes equations such that the flow remains parallel in an infinite pipe. Near the nozzle exit, however, small modifications of the profile occur.

As our interest is only the computation of a steady solution of the Navier–Stokes equations, the quality of the non-reflecting boundary conditions is not an issue in this case. We therefore use sponge layer to smoothly impose prescribed values for the flow variables at the boundaries. For $x = x_m$ and $r = r_M$, homogeneous Dirichlet conditions are used for the velocity while the density and temperature are set to 1. The outflow profile at $x = x_M$ is computed using a boundary layer approximation.

Figures 3 and 4 represent the axial velocity distribution for isothermal and hot ($S = 0.5$) jets at Re = 100 and Ma = 0.9, and for an shear layer thickness $\phi = 0.25$. In this case, the flow is stable to finite amplitude perturbations, and the steady state can be obtained by long time integration of the equations of motion. At higher Reynolds number however this is no longer the case as the flow exhibits a Kelvin-Helmholtz type instability. In these cases *selective frequency damping* (SFD) [1] proves efficient to numerically stabilize the flow and reach a steady state, provided the cutoff frequency of the algorithm is chosen to be smaller than the frequency of the non-linear oscillations.

2.4 Global modes computation

Global modes correspond to the temporal eigenvectors of the Navier–Stokes equations linearized around the previously determined base flow. The eigenvalue problem is solved using an Arnoldi algorithm. This method is effective for the computation of a few modes associated with the largest magnitude eigenvalues of a linear operator. In the case of the linearized Navier-Stokes equations, this corresponds either to modes with a large frequency or a large decay rate. These modes are spurious and have no physical significance. In order to compute physically relevant global modes, two types of transformations of the spectrum are commonly used. If only the most unstable modes are needed an exponential transform may be used, which is equivalent to computing the modes of the propagator [8]. If a more accurate picture of the spectrum is needed, the standard method is the shift-invert spectral transformation (or a variant called Cayley transformation). This allows to "zoom" into selected parts of the spectrum, but involves the inversion of a linear system at each iteration. This is usually done using a direct LU decomposition of the matrix associated with the Jacobian operator, whether in dense of sparse frameworks depending on the discretization technique employed [2, 3]. Such an approach, when large domains and high order differentiation schemes are involved (which results in a matrix with a large bandwidth), becomes extremely demanding in terms of memory. A matrix free version of this method has been proposed [13], using an iterative linear solver such as BiCGStab. In this case, poor conditioning of the transformed operator requires the use of a good preconditioner, which is also computationally expensive.

An alternative method has been developed for the present problem, in which temporal filtering is used to compute global modes in the vicinity of a prescribed real frequency. To this end, a band-pass frequency filter, similar to the SFD method described in reference [1], is applied to the linearized equations of motion. The most unstable eigenmodes of the filtered system are then retrieved by simple time-stepping. Details of this method will be described in a forthcoming paper.

The choice of well-suited numerical boundary conditions is critical for the success of the present computations, especially in view of accurate acoustic results. Such boundary conditions must minimize spurious acoustic reflections, and at the same time they must let vortical structures leave the computational domain without unphysical sound generation. Sponge layers, as described above, are widely used for such purposes in aeroacoustic computations. In addition, we apply the non-reflective conditions given by [5] on the outermost grid points. This formulation provides a convection of vortical perturbations across the downstream boundary, and it approximates acoustic waves as being of a spherical shape, emanating from a given point inside the domain, which here is taken to be the nozzle exit.

3 Results and discussion

3.1 Isothermal jet

Figure 5 represents some of the least stable eigenvalues of the isothermal jet, as computed with the new SFD method. Only a few selected frequency regions of the spectrum have been investigated, and the following discussion will focus on results obtained in the vicinities of real frequencies $\omega = 0.25$, 0.5 and 1. Note that not all results are fully converged; particularly the growth rate values still display a certain dependency on the computational domain size. However, the spatial structures of these global modes exhibit sufficiently consistent features to justify a qualitative discussion.

One family of global modes is denoted by red symbols in figure 5. Their eigenvalues are characterized by low frequencies, ranging from 0.15 to 0.55, and by temporal decay rates between -0.055 and -0.12. Within this family, the spatial structure of the perturbation eigenfunctions evolves slowly with the real frequency, and this evolution follows a consistent trend. Vorticity perturbations, defined as the curl of the velocity vector eigenfunctions, characterize the instability-driven aerodynamic near-field dynamics associated with a global mode. Real parts of the vorticity eigenfunctions are shown in figure 6a and b for the modes labeled 1 and 2 in figure 5 ($\omega_1 = 0.16 - 0.06\imath$ and $\omega_2 = 0.45 - 0.08\imath$).

The vorticity field of mode 1 (figure 6a), in the very low frequency regime, displays perturbations that are exponentially growing in the streamwise direction, both inside the pipe and in the free jet. Perturbations of the streamwise velocity u'_x within the pipe are shown separately in figure 7a. A peak amplitude

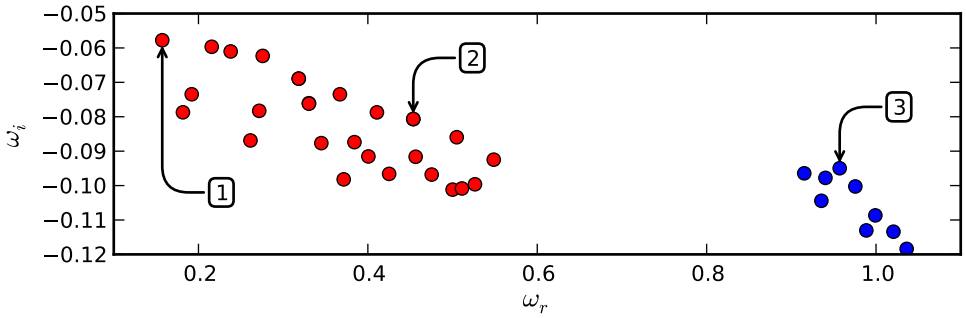

Figure 5: Eigenvalue spectrum for an isothermal jet at Re = 100 and Ma = 0.9 (axisymmetric modes). The spatial eigenmode shapes associated with labeled eigenvalues are represented in figures 6 and 7.

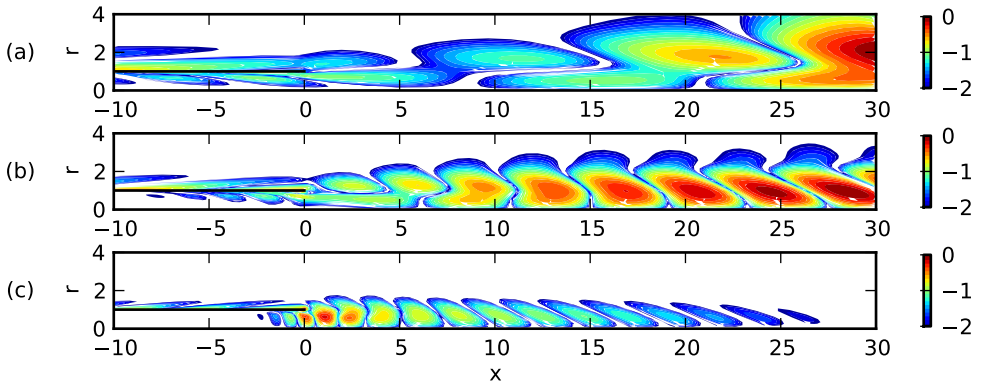

Figure 6: Spatial distribution of the perturbation vorticity $\log_{10}|\nabla \times \mathbf{u}'|$ in the near-field region for selected global modes of a isothermal jet at Re = 100 and Ma = 0.9. Figures (a) to (c) respectively correspond to modes 1 to 3, as labeled in figure 5. The full streamwise length of the physical domain is represented.

of u'_x near the wall seems to characterize these perturbations as a "wall mode" of the pipe flow. In the free jet, the vorticity perturbations form a regular pattern with local amplitude maxima on both sides of the $r = 1$ line. In an infinitely long domain, the amplitude would be expected to reach a maximum near the location where the base flow becomes stable, followed by streamwise decay. However, this maximum location appears to lie beyond the downstream boundary of the current physical domain. It has been demonstrated in [7] that the acoustic radiation from an instability wave packet critically depends on its precise spatial shape, even in the low-amplitude regions far away from the maximum. As a consequence, a meaningful discussion of the acoustic far-field in the present context will require a large computational domain that captures the entire length of the near-field wave packet.

The wavelength of vorticity perturbations shortens as the real frequency increases, such that a phase velocity around $c_{ph} = 0.4$ is maintained for all modes marked by red symbols in figure 5. The vorticity field of mode 2 is shown in figure 6b. The spatial structure immediately downstream of the nozzle strongly resembles that of mode 1, with amplitude maxima on both sides of the shear layer. Around $x = 10$, this shape smoothly transitions to a different pattern, with one single vorticity maximum along r, located near the radial position of maximum base flow shear. These perturbations continue to grow

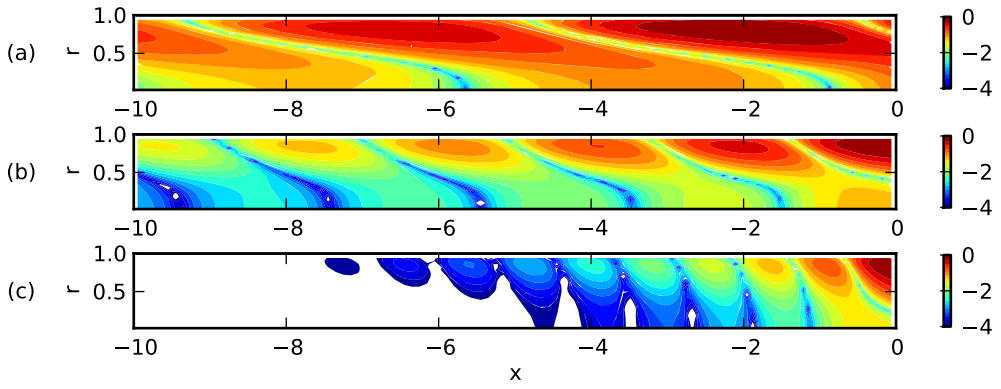

Figure 7: Spatial distribution of the streamwise perturbation velocity $\log_{10}|u'_x|$ inside the pipe. (a) mode 1; (b) mode 2; (c) mode 3; all as labeled in figure 5.

in the downstream direction. Although the spatial growth is only weak near the downstream boundary of the physical domain ($x = 30$), the amplitude maximum is again not captured in the present computations. Mode 2 velocity perturbations inside the pipe, shown in figure 7b, are very similar to those associated with mode 1, except for their shorter wavelength. All global modes of the present family (red symbols in figure 5) with frequencies $\omega_r > 0.25$ exhibit a similar spatial structure as discussed here for mode 2. The transition between the two distinct radial patterns of vorticity distribution continuously takes place further upstream as ω_r increases.

A second family of global modes is found near real frequencies $\omega_r = 1$, denoted by blue symbols in figure 5. The least stable of these is labeled mode 3 ($\omega_3 = 0.96 - 0.09\imath$), and its vorticity distribution is displayed in figure 6c. Perturbations in the free jet are concentrated around the center of the shear layer, and their amplitude decays immediately downstream of the nozzle exit. Their radial distribution strongly resembles the downstream part of mode 2. Velocity perturbations inside the pipe (figure 7c) again bear the same characteristic features of a wall mode as discussed for mode 1. It may indeed be speculated that the two families of global modes are not distinct, but form one single branch. This will have to be verified through further computations at intermediate frequencies.

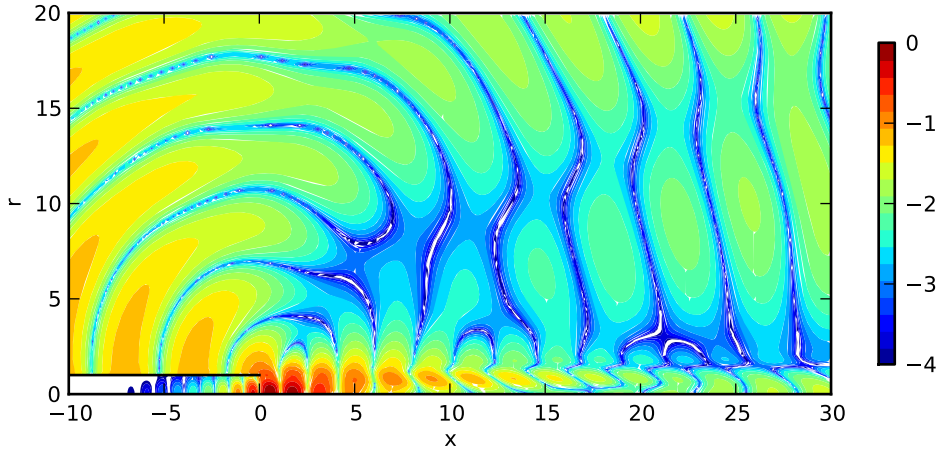

Figure 8: Dilatation field $\log_{10}|\nabla \cdot \mathbf{u}'|$ of mode 3, as labeled in figure 5. The entire extent of the physical domain is represented.

The compactness of near-field perturbations in the mode 3 case allows a discussion of the associated acoustic radiation. The acoustic far-field may be characterized by the dilatation in the outer stream, defined as the divergence of perturbation velocity. The dilatation field of mode 3, represented in figure 8, exhibits weak sound radiation at downstream angles, measured relative to the jet axis, and considerably stronger radiation at upstream angles. Both the upstream- and downstream-traveling waves apparently emanate from the nozzle exit. An extinction angle seems to be present in the downstream-radiating part of the far-field, measured as approximately 40° relative to the jet axis. The directivity pattern suggests that sound waves produced near the nozzle edge on one side of the jet axis are out-of-phase with those produced on the opposite side. Downstream radiation would then be affected by destructive interference, whereas in the upstream direction such interference would be prevented due to shielding by the pipe. This simple geometrical argument will need to be confirmed in a detailed study of aeroacoustic source term distributions.

However, the dilatation field displayed in figure 8 clearly shows evidence of spurious acoustic reflections from the numerical boundary conditions. In particular, the dilatation amplitude does not decay with distance ξ from the apparent source location at the expected rate of ξ^{-1}. At some radiation angles, the amplitude indeed increases with ξ. Further fine-tuning of the damping parameter inside the sponge regions is likely to remedy this problem in future computations.

3.2 Hot jet

Low-frequency modes have been computed for a heated jet ($S = 0.5$), with all other parameters identical as in the isothermal case. The spectrum is represented in figure 9 for frequencies $\omega_r < 0.55$. While all global modes in this frequency range remain stable, a new family of dominant modes is found, represented by purple symbols. These modes form a contiguous branch over the interval $0.3 < \omega_r < 0.52$. A second distinct set of modes, represented by light blue symbols, is detected at frequencies near $\omega_r = 0.5$. The dominant branch displays decay rates much closer to zero than those found for the isothermal jet, i.e. the hot jet is less stable over the investigated frequency range. This finding is consistent with experimental and numerical observations in jets at lower Mach numbers.

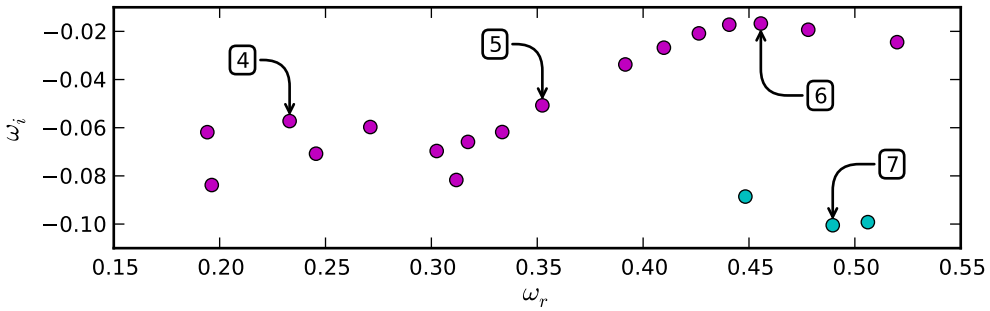

Figure 9: Eigenvalue spectrum for an hot jet at Re = 100, Ma = 0.9 and $S = 0.5$ (axisymmetric modes). The spatial eigenmode shapes associated with eigenvalues labeled 4 to 7 (respectively $\omega_4 = 0.23 - 0.06\imath$, $\omega_5 = 0.35 - 0.05\imath$, $\omega_6 = 0.45 - 0.02\imath$ and $\omega_7 = 0.49 - 0.1\imath$) are given in figure 10.

Figure 10 shows the vorticity distributions associated with selected eigenvalues (labels in figure 9). Mode 4 (figure 10a) is characterized by long-wavelength perturbations in the outer region of the jet, $r > 1$, as well as short-wavelength perturbations in the inner region, $r < 1$. Similar features are seen for modes 5 and 6 (figures 10b and c), which are found along the same mode branch at higher real frequencies. The phase velocity of perturbations in the outer jet region is around $c_{ph} = 0.6$ for all these modes, and the wavelength therefore shortens with increasing frequencies. The inner short-wavelength perturbations appear to follow an opposite trend. In the case of the least stable mode (mode 6, figure 10c), the wavelengths in the inner and outer jet regions are comparable. While the outer perturbations

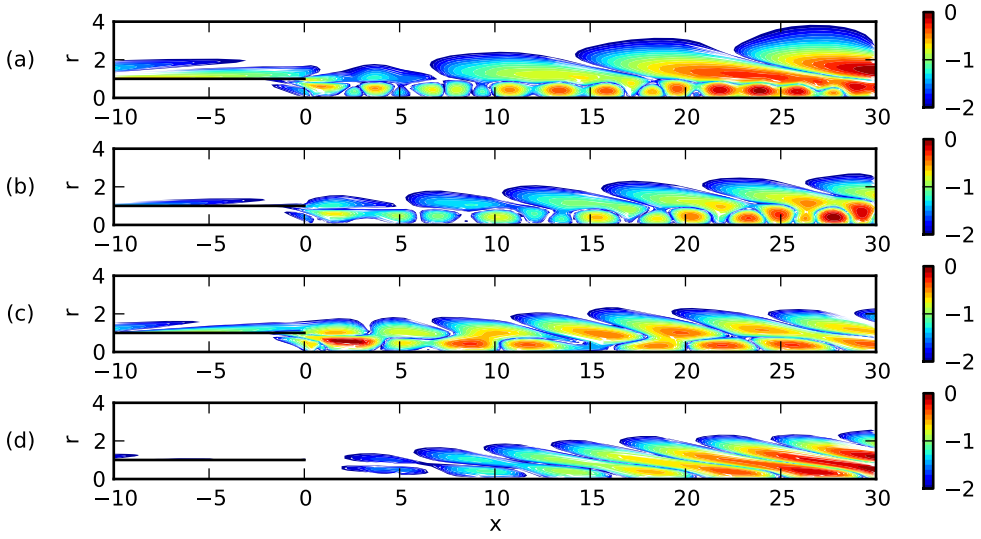

Figure 10: Spatial distribution of the perturbation vorticity $\log_{10}|\nabla\times\mathbf{u}'|$ for a hot jet at Re = 100, Ma = 0.9 and $S = 0.5$. Figures (a) to (d) correspond respectively to the eigenvalues labeled 4 to 7 in figure 9. The full streamwise length of the physical domain is represented.

may be said to be qualitatively similar to those of the isothermal jet, no interpretation of the inner perturbations can be offered at this point. However peculiar, their characteristic shape is consistently found in computations on different numerical grids.

Mode 7 represents the second family of global modes. Its near-field signature, shown in figure 10d, clearly sets it apart from the dominant mode branch. Close to the nozzle, the vorticity is concentrated in two maxima of opposite sign on both sides of the shear layer. Further downstream, pairs of diagonally opposite maxima of equal sign connect across the shear layer. The pairs finally form skewed continuous patches, vaguely reminiscent of the global mode shape in the isothermal jet at similar frequencies (figure 6b).

A discussion of acoustic radiation in the hot jet case is not attempted, since the computational domain does not include the wave packet maximum of any global mode at present.

4 Conclusion

A global stability analysis has been performed for one isothermal and one hot jet at low Reynolds number and high subsonic Mach number. A novel method has been employed to compute global modes using a time-stepping technique, which does not require the explicit solution of very large linear systems. Two families of stable global modes have been identified in each of the two jet configurations. In the isothermal jet, low-frequency modes exhibit spatial growth throughout the physical portion of the computational domain. The radial distribution of vorticity undergoes a smooth transition between two characteristic shapes, at a location that steadily moves upstream as the frequency increases and the associated wavelength decreases. This observation suggests that the dominant instability mechanism in the upstream portion of these modes requires the shear layer thickness to be small compared to the streamwise wavelength. Higher-frequency modes of the isothermal jet, around $\omega_r = 1$, exhibit spatial decay downstream of the nozzle exit. The vorticity distribution resembles that of the downstream portion of the lower-frequency modes. Whether these two mode branches are indeed distinct will have to be determined on the basis of further computations. Both have been seen to be connected to a wall

instability mode in the parallel pipe flow upstream of the nozzle.

The two global mode branches found in the hot jet are clearly distinct. The dominant branch displays a temporal decay rate close to neutrality near $\omega_r = 0.45$. The hot jet therefore is less globally stable than the isothermal jet. The vorticity perturbations associated with these slightly damped modes display structures of shorter wavelength near the center-line and structures of longer wavelength in the outer region of the jet. The physical nature of particularly the inner vorticity structures remains to be clarified. The second mode branch of the hot jet shows stronger temporal decay, but is characterized by very orderly vorticity waves.

The acoustic far-field has been presented only for one mode of the higher-frequency branch in the isothermal case. The strongest radiation is directed upstream, whereas extinction angles are present in the downstream portion of the acoustic field. This directivity pattern has been attributed to azimuthal interference effects, which are prevented in the upstream direction by acoustic shielding provided by the nozzle. All other global modes have been found to still experience spatial growth as they enter the downstream sponge region, and their dominant region of sound production is therefore not captured in the present simulations. We hope to soon be able to report further progress from computations on larger domains.

This work is being supported by a Ph.D. fellowship from DGA (France).

References

[1] E. Akervik, L. Brandt, D. S. Henningson, J. Hoepffner, O. Marxen, and P. Schlatter. Steady solutions of the Navier-Stokes equations by selective frequency damping. *Physics of Fluids*, 18(6):068102, 2006.

[2] E. Akervik, U. Ehrenstein, F. Gallaire, and D. S. Henningson. Global two-dimensional stability measures of the flat plate boundary-layer flow. *European Journal of Mechanics - B/Fluids*, 27(5):501 – 513, 2008.

[3] A. Barbagallo, D. Sipp, and P. J. Schmid. Closed-loop control of an open cavity flow using reduced-order models. *Journal of Fluid Mechanics*, 641(-1):1–50, 2009.

[4] C. Bogey and C. Bailly. Computation of a high reynolds number jet and its radiated noise using large eddy simulation based on explicit filtering. *Computers & Fluids*, 35(10):1344 – 1358, 2006.

[5] C. Bogey and C. Bailly. Three-dimensional non-reflective boundary conditions for acoustic simulations: far field formulation and validation test cases. *Acta Acustica united with Acustica*, 88:463–471(9), July/August 2002.

[6] T. Colonius. Modeling artificial boundary conditions for compressible flow. *Annual Review of Fluid Mechanics*, 36(1):315–345, 2004.

[7] D. G. Crighton and P. Huerre. Shear-layer pressure fluctuations and superdirective acoustic sources. *Journal of Fluid Mechanics Digital Archive*, 220(-1):355–368, 1990.

[8] W. S. Edwards, L. S. Tuckerman, R. A. Friesner, and D. C. Sorensen. Krylov methods for the incompressible Navier-Stokes equations. *J. Comput. Phys.*, 110(1):82–102, 1994.

[9] J. B. Freund. Noise sources in a low-reynolds-number turbulent jet at mach 0.9. *Journal of Fluid Mechanics*, 438(-1):277–305, 2001.

[10] C. M. Ho and P. Huerre. Perturbed free shear layers. *Annual Review of Fluid Mechanics*, 16(1):365–422, 1984.

[11] P. Huerre and P. A. Monkewitz. Absolute and convective instabilities in free shear layers. *Journal of Fluid Mechanics Digital Archive*, 159(-1):151–168, 1985.

[12] L. Lesshafft, P. Huerre, P. Sagaut, and M. Terracol. Nonlinear global modes in hot jets. *Journal of Fluid Mechanics*, 554:393–409, 2006.

[13] C. J. Mack and P. J. Schmid. A preconditioned Krylov technique for global hydrodynamic stability analysis of large-scale compressible flows. *Journal of Computational Physics*, 229(3):541–560, 2010.

[14] M. R. Visbal and D. V. Gaitonde. On the use of higher-order finite-difference schemes on curvilinear and deforming meshes. *Journal of Computational Physics*, 181(1):155 – 185, 2002.